Modeling approach and simulations of mechanical wall stress caused by thermal-spray impacting hot surfaces

Sayop Kim, Haris Mehraj, Taehoon Han, Tonghun Lee, Kenneth S Kim, Chol-Bum M Kweon, Je Ir Ryu

Modeling approach and simulations of mechanical wall stress caused by thermal-spray impacting hot surfaces

Sayop Kim[1], Haris Mehraj[1], Taehoon Han[2], Tonghun Lee[3],
Kenneth S. Kim[4], Chol-Bum M. Kweon[4], and Je Ir Ryu*[1,5]

[1]Division of Engineering, New York University Abu Dhabi, Abu Dhabi, United Arab Emirates
[2]Department of Mechanical Engineering, University of Suwon, Gyeonggi-do, South Korea
[3]Department of Mechanical Science & Engineering, University of Illinois at Urbana-Champaign, Urbana, IL, USA
[4]Combat Capabilities Development Command Army Research Laboratory, Aberdeen Proving Ground, MD, USA
[5]Tandon School of Engineering, New York University, Brooklyn, NY, USA

Abstract
This research introduces a new method for numerically assessing the mechanical effects caused by the impact of thermal spray on walls. The Spray-Induced Wall Stress (SIWS) model, proposed recently, accounts for the interactions between the spray and the wall, leading to the formation of wall stress within the Lagrangian spray modeling framework. The primary aim of this research is to provide a mathematical explanation of the underlying physics of the model and validate it against existing experimental data. The remainder of the study focuses on applying the model to hot-surface configurations, such as flat hot surfaces and ignition assistance devices like the glow plug system. The results demonstrate the mechanical impact of high-speed spray jet impacts, leading to stress on the rigid body of the system. This research emphasizes the effectiveness of the SIWS model in determining mechanical stress, an aspect lacking in current Lagrangian spray models.

Keywords
Spray, Wall Stress, CFD, Glow Plug, Hot Surface

Introduction

Many combustion-powered propulsion systems utilize direct-injection compression ignition (CI) systems, known for their high thermal efficiency. This efficiency advantage can also be applied to aviation sector [1,2]. However, designing jet-fuel-powered aircraft engines for high-altitude conditions is challenging due to the varying oxygen levels at different elevations, which can affect ignition control [3,4]. In addition, the strategic focus of aircraft CI engine development is limited by the requirement of the United States Department of Defense's Single Fuel Forward Policy [5], which mandates the predominant use of jet fuels. However, this restriction poses a challenge due to the low reactivity of jet fuels. This combination of low reactivity and high-altitude operation can lead to unstable engine combustion, characterized by uncontrollable ignition timing, misfires, knocking, and subsequent power loss [1,6]. Therefore, an ignition assistance (IA) device is preferred as an active ignition control strategy to address these issues.

Active ignition control strategies can be implemented using the thermal-energy deposit method, which involves the use of an ignition assistance (IA) device like a glow plug. With this approach, the electronically powered IA device generates a preheating ignition source

(referred to as a thermal boundary layer) in the combustion chamber before fuel injection. This method has been widely used in various land-based engine systems [7] for cold-start operations. Similarly, jet-fueled aircraft engines can benefit from this technique to actively manage ignition control during high-altitude operations. Recent experimental and numerical studies [8,9,10] have focused on applying IA systems for this purpose.

In contrast to the cold start process in land-based CI engines, the IA device's hot surface must remain activated continuously while the engine is running. Consequently, the IA device is subjected to a significantly intense thermo-mechanical cycle, leading to steep temperature and pressure variations on its surface. This operational scenario can result in mechanical breakdown, corrosion, oxidation, and short circuits in the major components of the IA device. Previous studies [10,11] have focused on compiling important durability analyses for the practical use of the IA device. Motily [10], in particular, highlighted the system's durability and evaluated the failure modes of the IA device equipped with a rapid compression machine (RCM), noting the possibility of mechanical breakdown of the IA device.

The IA device's crucial components are generally exposed to the high-impulse spray impingement and the subsequent high-temperature and high-pressure combusting flow. Thereby, the system body fatigue can be accelerated by the thermo-mechanical impact loading. Such a phenomenon can be described from a fluid-structure interaction (FSI) standpoint. To simulate these physics, modeling the FSI can be enabled by strategically integrating two numerical modeling platforms, computational fluid dynamics (CFD) and finite element analysis (FEA), namely the coupled CFD-FEA method. The CFD solver is responsible for describing the thermal-fluid elements flowing around the IA device. Then, the FEA solver can import the transient thermo-mechanical boundary conditions from the CFD simulations and sequentially solve the governing equations for thermoelastic solid materials of interest.

Recently, Kim et al. [12] exploited the CFD-FEA coupling workflow to characterize the impact of high-pressure spray flame on the stress behavior on the surface of the IA device. The novelty of their workflow can be acknowledged by the capability of capturing the spatiotemporal boundary conditions on the interface, which is a lacking feature in the traditional semi-empirical method. However, the CFD-FEA coupling strategy available to this date excludes the mechanical impact from the spray-wall impingement due to the lack of spray impulse calculation capability in their CFD routine. To address this feature, the authors [13] proposed the ARL Spray-Induced Wall Stress (ARL-SIWS) model. The model accounts for the spray-induced mechanical impact on the wall-stress build-up and the authors successfully demonstrated the model's functionality in capturing the relevant wall-stress behavior. The current analysis in this paper is designed to extend the previous study [13] in pursuit of addressing the thermal-spray impingement and subsequent mechanical wall stress in the use of various hot-surface device configurations. To the authors' best knowledge, this is the novel approach to enable the spray-impingement-induced mechanical impact in the practical engine operating system.

Spray-Induced Wall Stress Model: ARL-SIWS model

The SIWS model [13] follows the description of the Lagrangian discrete phase modeling. The model development leverages the user-defined function (UDF) capability of the CONVERGE CFD solver [14]. The UDF modifies the existing drop-wall interaction routine in CONVERGE and utilizes the predefined identifiers, namely '*film_flag'*, to track the impinging parcels as well as the post-impinging parcels, e.g., film parcel and splashed parcel, as illustrated in **Figure 1**. The drop-wall interaction routine in CONVERGE provides relevant post-impinging regimes, including rebound, slide, and splashing. Subsequently, it returns the post-impinging parcel's properties, such as size and velocity. Of the drop splashing models

available in CONVERGE, O'Rourke model [15] is used in this test to account for post-impingement drop size and velocity.

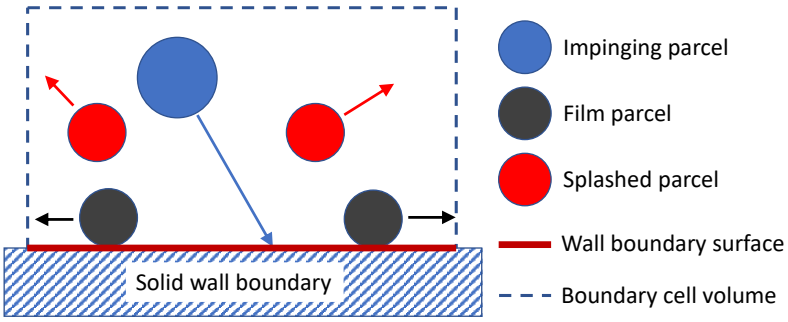

Figure 1 Schematic of impinging parcels (film_flag = 0) and post-impinging parcels (film_flag > 0: splashed parcels and film parcels) in the boundary cell adjacent to the solid wall.

The SIWS model's underlying assumption is based on the momentum transfer between computational parcels and wall boundaries. In this development routine, net force ($\vec{f}_{\text{net}}$) applied by a single parcel impingement is assumed to act on the embracing cell's wall boundary surface area (dA_{cell}). The wall-impingement event occurs in a characteristics impact time scale (dt_{impact}). Thus, the transmitted impulse to the cell boundary can be formulated as below:

$$\vec{I}_{\text{parcel}} = \vec{f}_{\text{net}} \cdot dt_{\text{impact}} \tag{1}$$

Provided that the impinging parcel is paired with the post-impinging parcel in the corresponding boundary cell, the impulse in Eq. (1) equates to momentum change ($d\vec{p}_{ij}$) between the pair, i and j, i.e., parcel identifiers for impinging and post-impinging parcels, respectively. As such, the total impulse acting on the boundary cell surface over the time step, dt, can be algebraically calculated by an integral of the momentum change for every pair of the parcels as expressed in Eq. (2). As the total force acting on the cell boundary surface is denoted by $\vec{F}_{\text{cell}}$ and impact time scale is dt, Eqs. (3, 4) derives the wall-stress component effective on the cell boundary surface area. Here, an empirical constant, C_{eff} , is employed to address a dynamic conversion efficiency. In the present test, this constant was set to be unity, which assumes no dynamical energy loss while transferring the momentum.

$$\vec{I}_{\text{cell}} = \sum_{ij} \vec{I}_{\text{parcel},\,ij} = \sum_{ij} dp_{ij} \tag{2}$$

$$\vec{I}_{\text{cell}} = \vec{F}_{\text{cell}} \cdot dt \tag{3}$$

$$\vec{\tau}_{\text{cell}} = \frac{C_{\text{eff}}\,\vec{I}_{\text{cell}}}{dt \cdot dA_{\text{cell}}} \tag{4}$$

Simulation Setup

In this section, two different test campaigns are adopted. The first test is designed for model validation using single-hole diesel injectors. The tested spray configurations include freely evolving sprays without impingement and wall-impinging sprays. Then the second test

inherits this best practice and subsequently adopts the RCM combustion chamber domain with the IA device equipped.

Using the CONVERGE CFD solver, 3-D Reynolds-Average-Navier-Stokes (3-D RANS) simulations were performed. Computational domains used in this work were constructed with the consistent meshing strategy, i.e., 8 mm of base grid-scale and 0.125 mm of minimum grid-scale achieved from a multi-level adaptive mesh refinement (AMR) strategy and a fixed embedding mesh embracing the high-speed spray jet plume. Such an optimized minimum grid scale was achieved by performing the preliminary grid sensitivity study as examined in **Figure 2** (See right plot). In the Lagrangian spray modeling aspect, computational parcels are injected through the nozzle hole into the domain. Subsequent atomization was accounted for by adopting Kelvin-Helmholtz-Rayleigh-Taylor (KH-RT) model [16].

The model validation test is spared to demonstrate the proposed SIWS model's functionality in determining the relevant scale of spray mechanical impact on the wall. The simulation results are compared with high-pressure diesel injector experiments that measured the momentum flux using the pressure transducer equipment downstream of the injector nozzle presented by Payri et al. [17]. Of their test conditions, the present work employs the test conditions available for the momentum flux measurements, as summarized in Table 1. In pursuit of the additional thermal-spray impingement test, the ambient air temperature was elevated for the virtual test using 500K, 700K, and 900K, and the surface temperature was set up accordingly to exclude the thermal boundary layer impact.

Table 1 Test conditions used for ARL-SIWS model validation

Injector ID	A	B	C
Nozzle hole diameter [μm]	112	137	156
Injection pressure [MPa]	30 and 80		
Ambient pressure [MPa]	3.5		
Ambient air temperature [K]	300		
Injection duration [ms]	2.0		

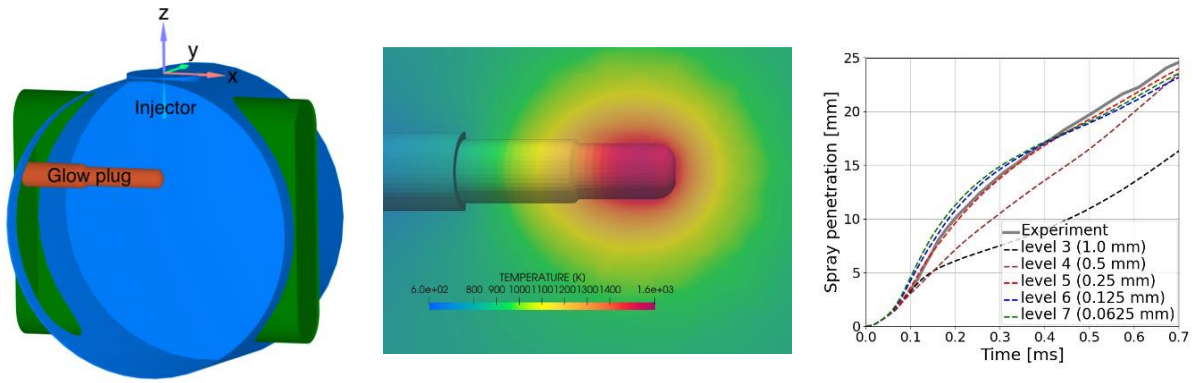

Figure 2 Geometrical configuration of the combustion chamber domain with injector and ignition assistance device (left) and thermal boundary layer generated by the electric circuit voltage input, 7V (middle), preliminary test on grid convergence setup using adaptive mesh refinement (AMR)

Additional 3-D RANS simulations were performed adopting the RCM combustion chamber domain [12,13]. The combustion chamber consists of a fuel injector. The employed fuel type was F-24 jet fuel, which is a conventional Jet-A fuel with military additives. The IA device in this test is a BERU glow plug and is longitudinally inserted into the domain, and its end-tip is situated 1 mm off from the injector axis. By shifting the vertical location, three

different downstream locations, 11 mm, 16 mm, and 21 mm, were considered. Only the non-reacting condition was configured by filling the chamber domain with intact nitrogen gas. The IA device was used to form a thermal boundary layer by applying a relevant electric circuit voltage input. In this test, non-thermal boundary layer case (0V) and thermal boundary layer case (4V) were considered. **Figure 2** illustrates the employed RCM combustion chamber domain and the thermal boundary layer surrounding the IA device according to the 7V input. The previous study details the RCM chamber dimension and IA device configuration [12].

Results and Discussions

The following analysis presents the rate of momentum estimated by the SIWS model compared to the measurement [17]. The test was performed by employing an impinging spray configuration at a 5 mm impact distance. In the corresponding experiment, a pressure transducer provides a stagnation wall to be impacted by the impinging spray and measures the spray impulse. The measured data presents the rate of momentum expressed in a unit of force [N]. **Figure 3** shows a comparison between the simulations and the measurements. The simulated results using the SIWS model agree well with the measurement in general. However, a certain error level appears to be induced using the Injector C, which is equipped with a larger injector nozzle diameter. This behavior is likely attributed to the simplified assumption made in the SIWS model. The model lacks the incorporation of complex physics involved in the deformation and breakup of large-volume droplets.

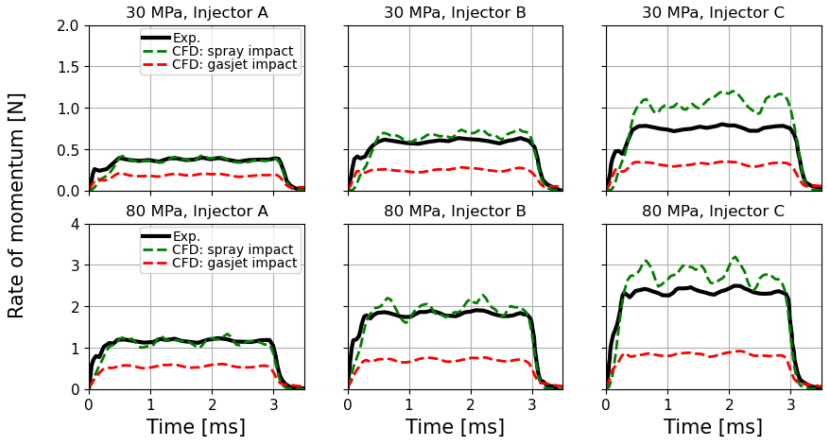

Figure 3 Comparison of the rate of momentum between the current CFD setup and the experiment [17]

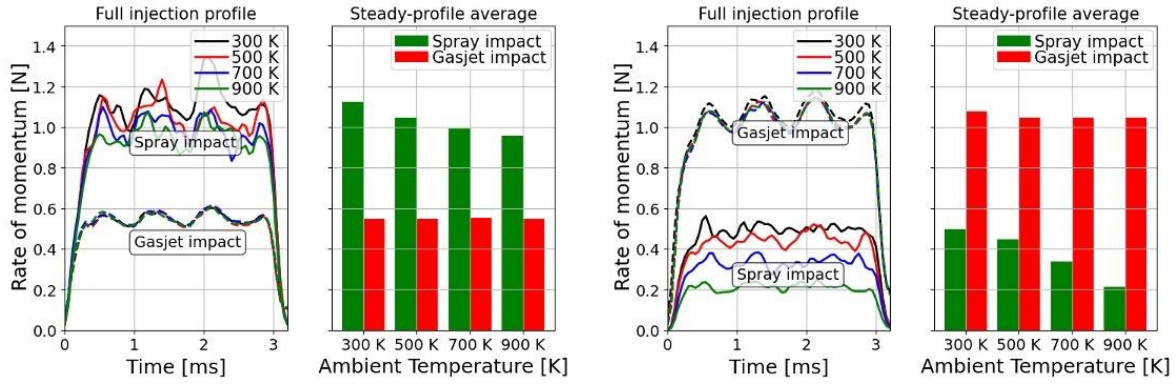

(a) Impact distance 5 mm (b) Impact distance 10 mm

Figure 4 Effect of ambient temperature on the rate of momentum, Injector A at 80 MPa of injection pressure.

It is important to note that a high-speed turbulence gas-jet can be established alongside the high-pressure spray jet, referred to as high-flux gas entrainment. As a result, both the spray-jet and the gas-jet mechanically impact the wall simultaneously. It is also important to emphasize that the effective rate of momentum of the gas-jet becomes marginal since the high-flux of gas flow produces low-pressure impact after impinging the stagnation point, thereby the effective impulse from the complete gas-jet flow becomes small [13]. However, the current analysis focuses on the locally impacted gas-jet impulse.

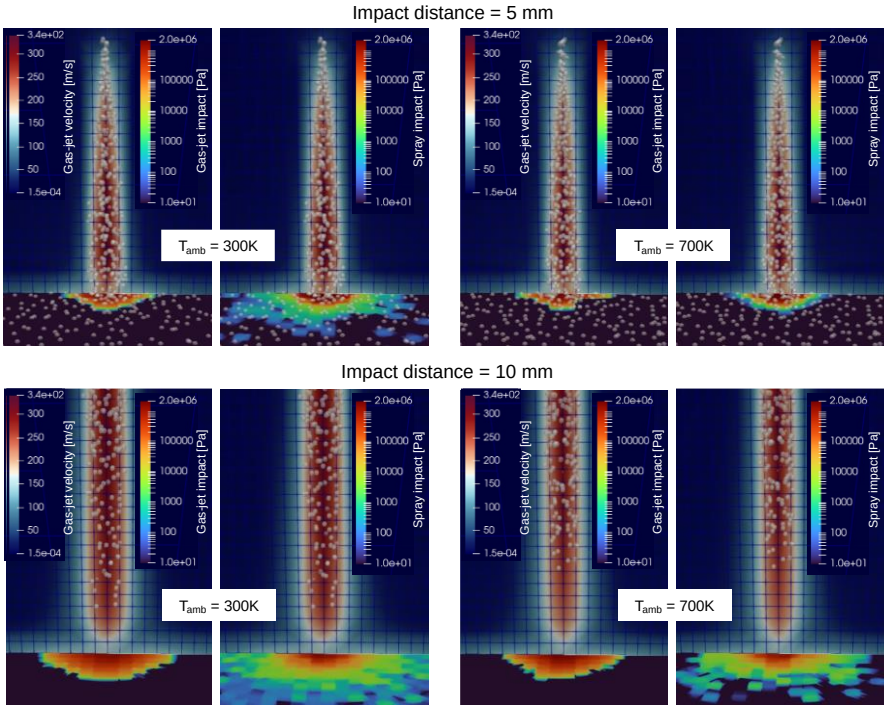

Figure 5 Spray-jet and gas-jet induced wall stress at two impact distance cases.

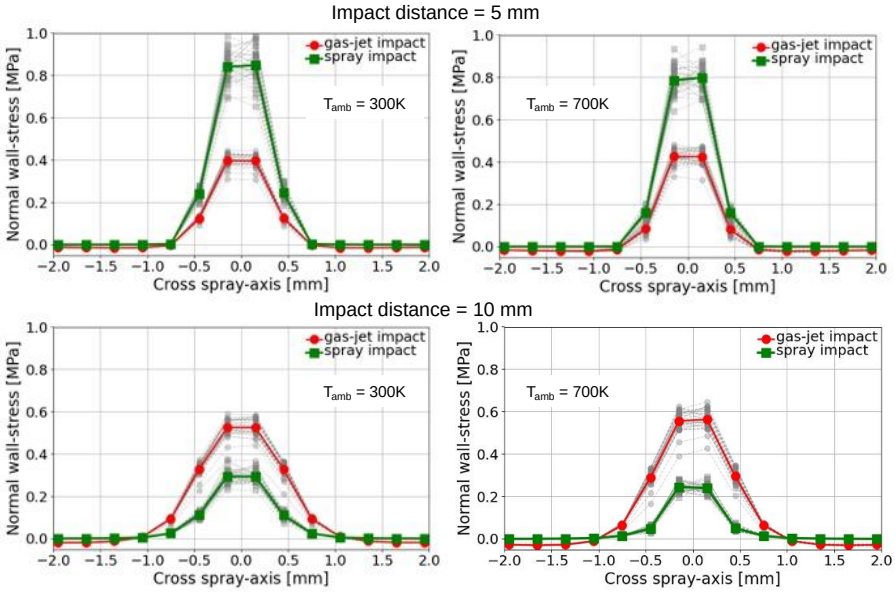

Figure 6 Time-averaged wall-stress distribution in a cross spray-axis direction.

Figure 4 summarizes the ambient temperature effect on the obtained rate of momentum in terms of gas-jet and spray-jet impulses. Two different impact distances are adopted in this analysis. In general, elevating ambient temperature holds a significant impact on the spray-

induced rate of momentum, i.e., impulse. The increased impact distance presents a counter-impact on the spray-induced impulse while increasing the gasjet-induced impulse. Further details will be discussed in the following wall-stress analysis.

Following analysis presents propensity of the spray-jet and gas-jet induced wall stress using the injector A and injection pressure of 80 MPa at two different impact distance 5 mm and 10 mm. In **Figure 5**, the wall stress induced by the spray impingement is contour-colored. The gas-jet impingement drives another wall stress component, a form of gas static pressure applied to the wall. **Figure 6** shows the time-averaged wall-stress distribution in terms of the separate impact of the gas-jet and the spray-jet. Each point-wise measurement is defined at 0.3 mm space apart in the cross-spray direction. Light gray-color dots indicate instantaneous wall-stress profile at 0.1 ms time intervals.

Specific details in the result vary depending on the impact distance and ambient temperature. Generic propensity follows the same trend as shown in **Figure 4**. The higher stress is contributed from the spray jet impingement at lower impact distance setup, whereas the increased impact distance reduces the spray-induced wall stress. Despite the marginal change seen in **Figure 5**, the increased ambient temperature (300K to 700K) appears to affect the wall-stress as well. The gas-jet impact presents higher wall stress at the higher ambient temperature, whereas the counter effect is obtained in the spray-induced wall stress. This propensity can be related to the liquid atomization performance in the near-wall region.

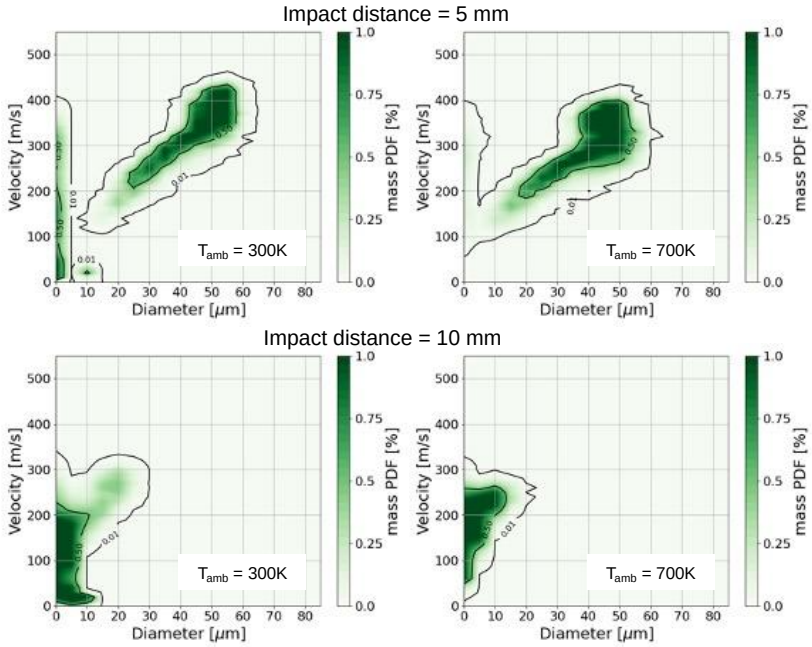

Figure 7 Joint PDFs of spray particle diameter and velocity using injector A at 80 MPa of injection pressure.

Figure 7 shows the joint PDF (probability density function) in terms of particle velocity and size. Liquid parcels in the boundary cells before wall contact are collected. It is important to identify the bimodal size distribution in the diameter axis that becomes prominent at the impact distance of 5 mm. Each group represents child parcels by the KH-RT breakup model [16] and parent parcels that have undergone the spray jet-breakup process in the intact core region. This indicates that the spray still undergoes within the distance of 5 mm, whereas the spray reaches a substantially atomized regime at 10 mm of impact distance. For that reason, the more minor spray-induced wall stress is attributed to the impact of substantially small liquid particles. On the other hand, increased ambient temperature holds counter impact. The

increased temperature accelerates the small particle evaporation; thereby, the slightly increased spray-induced wall stress is attributed to the large-sized particle group.

A meaningful structure analysis of the ignition assistance device component becomes possible with the aid of the SIWS model, allowing to quantify the stress level due to the direct wall contact of the spray jet. Additional wall-stress source comes from the gas phase pressure adjacent to the wall. In this test, the tip of the ignition assistance device heating element is located 11 mm, 16 mm and 21 mm downstream of the injector nozzle. Therefore, the different spray-jet-induced wall stress levels can be observed depending on the impact distance.

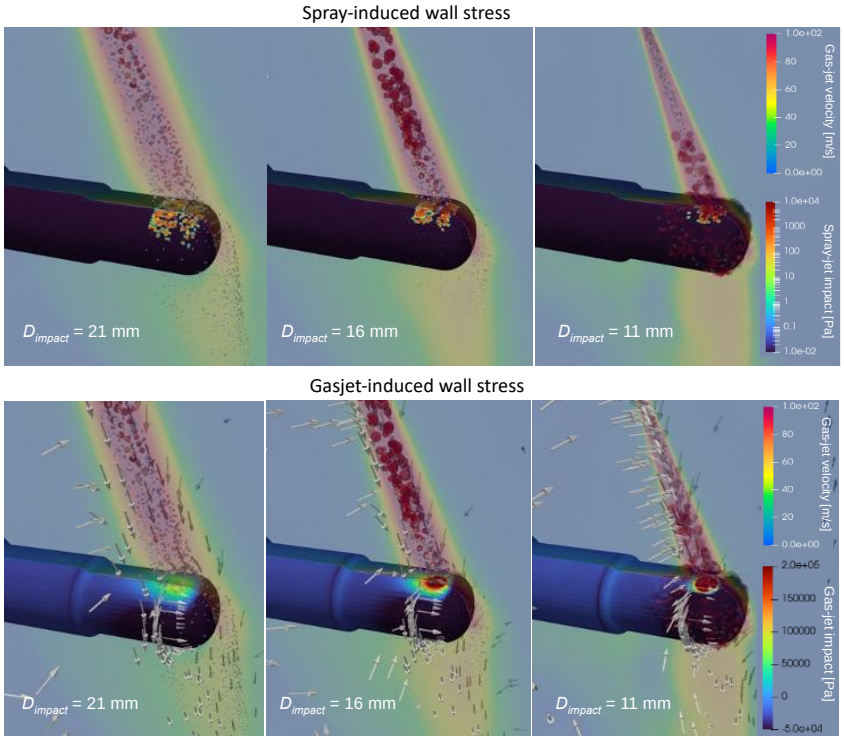

Figure 8 Spray-jet-induced and gas-jet-induced wall stress formation under non-reacting conditions.

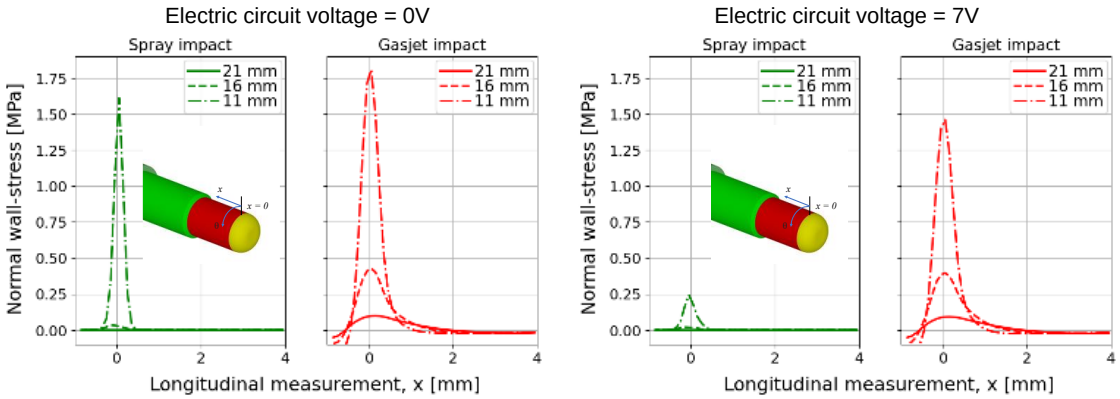

Figure 9 Wall-stress distribution response to the IA device hot surface (0V: 800K constant temperature, 7V: thermal boundary layer generated)

Figure 8 shows the normal component of the spray-jet-induced and the gas-jet-induced stress on the IA device after 1.5 ms of the start of injection. At an impact distance of 11 mm, the stress level is concentrated in a small impacting zone with a finite level, whereas the further downstream (e.g., 21 mm) makes the impacting zone wider due to the radially evolving spray

plume shape. At the same time, the stress level decreases when it impacts at 21 mm, as the momentum of the spray-jet has reduced in such a farther downstream location.

The gas-jet-induced wall stress in **Figure 8** is a continuous phase static pressure contribution. The stress level varies from positive value to negative value. The positive stress at the impacting zone indicates that the gas-jet impacts on that spot, creating a stagnation point. Meanwhile, due to the cylindrical shape of the ignition assistance device body, the gas-jet then sweeps around the body, as illustrated by the arrow-indicated stream. Such a high-velocity tangential to the surface leads to a pressure drop below the ambient pressure. As a result, negative relative pressure is observed continuously outside the stagnation point.

Figure 9 presents the hot-surface impact and the effect of impact distance on the wall-stress distribution. Unlike the previous spray-impingement test, the IA device hot-surface employs a temperature gradient in the near-wall region. Such a thermal boundary layer plays a role in mitigating the wall stress for both spray and gasjet contributions. The spray-induced wall stress is marginal at the reference impact distance (21 mm) because the liquid spray was fully atomized and vaporized [12].

Conclusions

This study introduces a novel approach in wall-stress evaluation with consideration of the spray-induced mechanical impact. The proposed SIWS model was successfully embedded into a Lagrangian spray modelling framework and adequately captures the experimentally observable spray momentum rate. This study extended the focus in evaluating the thermal-spray-induced wall stress by employing the different level of hot-surface temperature as well as different impact distance. The simulation results indicate that the wall stress induced by the spray jet can be as significant as the impact from the gas-jet when the impact distance is short. This high level of wall stress is concentrated in a small area of the spray-impinging region. From a structural analysis perspective, the SIWS model offers an effective solution. The simulated outcomes emphasize that the high-pressure spray jet has the potential to generate intense and localized wall stress accumulation. This, in turn, may lead to fatigue in the solid materials and ultimately result in system failure.

Acknowledgement

The SIWS model, known as the ARL-SIWS model, was developed by Dr. Sayop Kim during his post-doctoral appointment at Argonne National Laboratory. The research was supported by the Army Research Laboratory under Cooperative Agreement Number W911NF-18-2-0282. The simulations were conducted using the High-Performance Computing resources at New York University Abu Dhabi, with academic license support provided by Convergent Science.

References

[1] K. S. Kim, M. T. Szedlmayer, C.-B. M. Kweon, K. Kruger, J. A. Gibson, C. A. Lindsey, R. D. Meininger, M. R. Musser and A. V. Giddings, "The Effect of Outside Air Temperature and Cetane Number on Combustion and Performance in a UAV Diesel Engine at Various Altitude Conditions," in 53rd AIAA/SAE/ASEE Joint Propulsion Conference, Atlanta, GA, 2017

[2] L. Chen, M. Raza and J. Xiao, "Combustion Analysis of an Aviation Compression Ignition Engine Burning Pentanol–Kerosene Blends under Different Injection Timings," Energy & Fuels, vol. 31, no. 9, pp. 9429-9437, 2017

[3] Z. Kan, Z. Hu, D. Lou, P. Tan, Z. Cao and Z. Yang, "Effects of Altitude on Combustion and Ignition Characteristics of Speed-Up Period during Cold Start in a Diesel Engine," Energy, vol. 150, no. 1, pp. 164-175, 2018

[4] B.-X. Lin, Y. Wu, M.-X. Xu and Y.-M. Shen, "Experimental Investigation on High-Altitude Ignition and Ignition Enhancement by Multi-Channel Plasma Igniter," Plasma Chemistry and Plasma Processing, vol. 41, pp. 1435-1454, 2021
[5] "DoD Management Policy for Energy Commodities and Related Services Section 4.2: Fuel Standardization," U.S. Department of Defense, Directive 4140.25, Washington D.C., 2004.
[6] R. D. Meininger, C.-B. M. Kweon, M. T. Szedlmayer, K. Q. Dang, N. B. Jackson, C. A. Lindsey, J. A. Gibson and R. H. Armstrong, "Knock Criteria for Aviation Diesel Engines," International Journal of Engine Research, vol. 18, no. 7, pp. 752-762, 2016
[7] Q. Li, P. Shayler, M. McGhee and A. La Rocca, "The Initiation and Development of Combustion under Cold Idling Conditions Using a Glow Plug in Diesel Engines," International Journal of Engine Research, vol. 18, no. 3, pp. 240-255, 2017.
[8] E. R. Amezcua, K. Kim, D. Rothamer and C.-B. Kweon, "Ignition Sensitivity Analysis for Energy-Assisted Compression-Ignition Operation on Jet Fuels with Varying Cetane Number," SAE International Journal of Advances and Current Practices in Mobility, vol. 4, no. 5, pp. 1651-1666, 2022.
[9] J. I. Ryu, A. H. Motily, T. Lee, R. Scarcelli, S. Som, K. S. Kim and C.-B. M. Kweon, "Ignition of Jet Fuel Assisted by a Hot Surface at Aircraft Compression Ignition Engine Conditions," in AIAA Propulsion and Energy Forum, 2020.
[10] A. H. Motily, "Evaluation of Hot Surface Ignition Device Performance with High-Pressure Kerosene Fuel Sprays," in M.S. Dissertation, Urbana-Champaign, IL, Department of Mechanical Science and Engineering, University of Illinois at Urbana-Champaign, 2020.
[11] B. Karpe, D. Klobčar, J. Kovač, M. Bizjak, B. Kosec and S. Veskovič-Bukudur, "Failure Analysis of Diesel Engine Glow Plugs," Engineering Failure Analysis, vol. 109, p. 104394, 2020.
[12] S. Kim, J. I. Ryu, S.-G. Kang, A. H. Motily, P. Numkiatsakul, R. Alosno, W. M. Kriven, K. S. Kim and C.-B. M. Kweon, "Numerical Investigations of Combustion Dynamics and Thermo-Mechanical Stress in the Ignition Assistance System for Small Aircraft Engines," Combustion Science and Technology, 2023.
[13] S. Kim, R. Torelly, S. K. Oruganti, J. I. Ryu, T. Lee, K. S. Kim and C.-B. M. Kweon, "Modeling of the Spray-Induced Wall Stress Acting on the Ignition Assistance Device," Physics of Fluids, vol. 35, no. 10, p. 103325, 2023.
[14] K. J. Richards, P. K. Senecal and E. Pomraning, "CONVERGE 3.0.27," Convergent Science, Madison, WI, 2023.
[15] P. J. O'Rourke and A. A. Amsden, "A Spray/Wall Interaction Submodel for the KIVA-3 Wall Film Model," SAE Journal of Engines, vol. 109, no. 3, pp. 281-298, 2000.
[16] J. C. Beale and R. D. Reitz, "Modeling Spray Atomization with the Kelvin-Helmholtz/Rayleigh-Taylor Hybrid Model," Atomization and Sprays, vol. 9, no. 6, pp. 623-650, 1999.
[17] [17] R. Payri, S. Ruiz, F. J. Salvador and J. Gimeno, "On the Dependence of Spray Momentum Flux
[18] in Spray Penetration: Momentum Flux Packets Penetration Model," Journal of
[19] Mechanical Science and Technology, vol. 21, pp. 1100-1111, 2007